Materials
Horizons

COMMUNICATION

View Article Online
View Journal | View Issue

Cite this: *Mater. Horiz.*, 2025, **12**, 1558

Received 13th September 2024,
Accepted 21st November 2024

DOI: 10.1039/d4mh01266f

rsc.li/materials-horizons

Space-confined mediation of electron transfer for efficient biomolecular solar conversion†

Margot Jacquet, *[a] Miriam Izzo, [a] Piotr Wróbel, [b] Marcin Strawski, [c]
Massimo Trotta, [d] Rafał Jurczakowski [e] and Joanna Kargul *[a]

Solar-converting nanosystems using self-renewing biomaterial resources carry great potential for developing sustainable technologies to ameliorate climate change and minimize reliance on fossil fuels. By mimicking natural photosynthesis, diverse proof-of-concept biosolar systems have been used to produce green electricity, fuels and chemicals. Efforts so far have focused on optimizing light harvesting, biocatalyst loading and electron transfer (ET), however, the long-term performance of best-performing systems remains a major challenge due to the intensive use of diffusive, toxic mediators. To overcome this limitation, we developed a rationally designed nanosystem based on the entrapment of non-toxic mediator, ferrocene dimethanol (Fc), localized at the abiotic–biotic molecular interface that efficiently promoted ET between electrode surface and two photosynthetic proteins: cytochrome *c* and photosystem I. We demonstrate that space-confined Fc mediators (1 nM) are as effective in terms of ET kinetics as a 500 000-fold higher concentration of freely-diffusive Fc. The Fc-confined biophotocathodes showed a milestone photocurrent density of 14 μA cm^{-2} under oxic conditions compared to analogous planar (2D) biophotoelectrodes, with a photoconductive biolayer stable for over 5 months. The space-confined ET mediation reported in this work opens a new avenue for efficiently interfacing biomachineries, providing a benchmark design advancement in the quest for viable biohybrid technologies.

New concepts

We report the discovery of an innovative and sustainable biomolecular nanosystem for efficient direct electron transfer (ET) in which the novel abiotic–biotic interface is based on a non-toxic, space-confined carbonaceous redox mediator. Whilst biohybrid materials had emerged as promising alternatives to purely synthetic materials in a vast range of applications ranging from solar cells to catalysis and sensing, the effective electrical wiring of the enzymes to electrode materials remains a key challenge to achieve high performance of such systems in the long term. The system with the nM concentration of space-confined ferrocene in the biomolecular interface outperformed the analogous system with the freely diffusing mediator used in a μM range in terms of significantly faster ET kinetics and higher photocurrent output and stability. As such, the new concept of space-confined mediators overcomes the limitations of mass transfer commonly used in the biomolecular systems to boost their performance. It also provides a true milestone in the development of sustainable and viable biomolecular conversion systems.

Introduction

Integrating natural molecular machines into advanced functional materials is an important burgeoning strategy toward a sustainable future whereby ever-growing energy demand can be satisfied with a carbon-neutral or even carbon-negative footprint. Natural photosynthesis provides a blueprint in the quest for the construction of viable artificial and semi-artificial solar conversion devices.[1] Although mimicking natural photosynthesis has inspired scientists for decades since the seminal work of Fujishima and Honda[2] spawning a plethora of technologically advanced artificial solar conversion systems, so far Solar-to-X technologies have not been implemented at scale mainly due to the use of expensive, toxic, and underperforming in the long-term catalytic materials.[3–6] In contrast, semi-artificial photosynthesis aims to overcome the limitations of fully artificial photosynthetic systems by using whole cell biocatalysts, enzymes or even light-gated biomachineries[7–9] to obtain the desired reaction. Numerous biosolar proof-of-concept prototypes have been developed for the production of green

---

[a] *Solar Fuels Laboratory, Centre of New Technology, University of Warsaw, Banacha 2C, 02-097 Warsaw, Poland. E-mail: m.jacquet@cent.uw.edu.pl, j.kargul@cent.uw.edu.pl*
[b] *Faculty of Physics, University of Warsaw, Pasteura 5, 02-093 Warsaw, Poland*
[c] *Faculty of Chemistry, Biological and Chemical Research Centre, University of Warsaw, Żwirki i Wigury 101, 02-089 Warsaw, Poland*
[d] *Institute for Physical Chemical Processes, National Research Council, E. Orabona 4, 70125 Bari, Italy*
[e] *Electrochemistry of New Materials, Centre of Biological and Chemical Sciences, Faculty of Chemistry, University of Warsaw, ul. Żwirki i Wigury 101, 02-089 Warsaw, Poland*

† Electronic supplementary information (ESI) available. See DOI: **https://doi.org/10.1039/d4mh01266f**

electricity, and in some cases also renewable fuels.[10–12] Among the different solar-driven enzymes, photosystem I (PSI) is by far the biophotocatalyst of choice due to its exceptional inherent photochemical properties (quantum yield of unity, long-lived charge-separated state $P700^{+}F_{B}^{-}$, and highest known natural reducing potential) together with its remarkable thermal and pH stability upon its isolation from the natural environment of photosynthetic membranes.[13] Whilst PSI functionality has been optimized throughout over 2 billion years of evolution, the successful implementation of PSI in solar-converting technologies relies on a rational nanoengineering of efficient electron transfer (ET) between PSI and electrode surface.[14,15] Specifically, to exploit the potentiality of PSI in biophotovoltaic devices, the optimization of the abiotic–biotic molecular interface is essential to ensure forward electron transfer while minimizing wasteful back reactions and short-circuiting. Additionally, a uniform and ordered orientation of PSI, acting as a natural photodiode, is essential for obtaining a well-controlled anisotropic ET. Although increasingly efficient devices have been reported, notably those with 3D nanostructured electrodes for improved PSI loading and light absorption,[16–18] few examples have actually applied the controlled interfacing of PSI with the electrode surface. Instead, the best-performing systems have resorted to the use of freely-diffusing toxic mediators and mass transfer processes to sustain PSI functionality,[19,20] thus precluding a large-scale implementation. Some systems have been devised to address this major drawback by developing redox-active polymeric interfaces, albeit they suffer from the lack of stable immobilization of oriented proteins,[21,22] and reliance on toxic mediators to boost the performance.[23,24]

Here, we report a simple and sustainable approach for efficiently interfacing PSI with a cost-efficient planar transparent electrode. By rationally designing the molecular interface for stable orientation of PSI[25] and enhanced anisotropic ET[26] (Fig. 1), we demonstrate the successful application of space-confining an innocuous and unexplored redox mediator: ferrocene dimethanol (Fc) within the abiotic–biotic interface to significantly improved photocurrent production and long-term stability of the photoconductive biolayer. We show that the Fc-confined biophotocathode remarkably outperforms the Fc-free counterpart, even in the presence of increasing amounts of freely diffusive Fc. This approach provides a breakthrough in the quest for viable biosolar and bioelectronic technologies, by space-confining ET mediation at the abiotic–biotic interface, thus preventing the limitations of diffusive mediators and their competitive interference with complex electrolytes when applied for solar fuel production, biocatalysis and biosensing.

Results and discussion

Preparation of PSI biohybrid electrodes

For efficiently interfacing PSI on fluorine-doped tin oxide (FTO), the bio-organic interface was employed comprising a covalent diazonium-based molecular wire shown previously to promote improved directional electron transfer[26] and terminated with the nickel–nitrilotriacetic acid (NTA) complex for stable binding of His_6-tagged cytochrome c_{553} (cyt *c*). The latter electroactive protein serves as a natural electron donor to the photochemical reaction centre of PSI. As cyt *c* interacts with PSI in a domain-specific manner, it can serve to orient PSI with its reaction centre towards the electrode surface[25,27] and to ensure directional cathodic ET, *i.e.* from the electrode to PSI.[26] The PSI-based biophotocathode was constructed following the previously optimized step-by-step procedure,[25,26] as shown in Fig. 1a. Briefly, the FTO surface was first covalently functionalized *via* the electrografting of an aryl diazonium salt bearing a protected alkyne with trimethylsilyl (TMS) group (Fig. S1, ESI†). After the deprotection step with tetrabutylammonium fluoride (TBAF), the NTA moiety was bound to the wire by the click chemistry reaction between the terminal alkyne and azide group of the NTA derivative. Following an EDTA treatment to remove the residual copper traces from the alkyne–azide cycloaddition step, nickel cations were added to form the Ni–NTA complex for covalent anchoring of His_6-tagged cyt *c* *via* metal affinity, allowing the final electrical wiring[28] and oriented immobilization of PSI[25,27] due to the molecular recognition between both protein interactors.

The stepwise preparation of the abiotic FTO-*c*NTA-Ni (Fig. S2, ESI†) and biotic architectures FTO-*c*NTA-Ni-cyt (Fig. S2, ESI†) and FTO-*c*NTA-Ni-cyt-PSI (Fig. 1b) was followed by measuring electrochemical impedance spectra (EIS) in the presence of the redox probe 1,1′-ferrocenedimethanol (Fc) and examining the variation of the charge transfer resistance R_{CT} and the double-layer capacitance C_{dl} parameters (Table S1, ESI†). The tendency observed until the nickel metalation is fully in line with our previously reported observations,[26] confirming the covalent functionalization as well as its homogeneity as shown by atomic mapping of nickel atoms by secondary ion mass spectrometry (SIMS) (Fig. 1c). As expected, subsequently to the immobilization of cyt *c* and PSI proteins, a significant increase of the R_{CT} parameter was recorded owing to the dense protein backbone hindering the interfacial ET pathway between the electrode and diffusive Fc probe. Interestingly, the attachment of the proteins resulted in a slight increase of the C_{dl} and the Φ parameters (Table S1, ESI†), confirming the formation of a well-ordered bio-organic architecture.[29]

The effective electrical wiring of redox-active cyt *c* was investigated by cyclic voltammetry (CV) in aqueous phosphate buffer (PB, pH 7). Importantly, following the EIS experiments, a ''residual'' redox signal originating from the Fc probe was systematically detected despite meticulous cleaning between each functionalization step. Therefore, freshly-made electrodes were prepared without the stepwise EIS characterization. As shown in Fig. 1d, the presence of cyt *c* leads to the appearance of a redox signal at $E_{1/2} = 0.29$ V *vs.* Ag/AgCl, which is attributed to the Fe^{III}/Fe^{II} couple from the heme group of cyt *c*, attesting ET through the molecular wire. By analysing the current peak intensity of ET (I) at different scan rates (ν), the covalent binding of cyt *c* was confirmed from the obtained linear dependency $f(\nu) = I$ (inset Fig. 1d) with a surface coverage (Γ) of 9.85×10^{-12} mol cm^{-2} (see Experimental section). The interfacial ET rate constant (k_{ET}) was determined from the

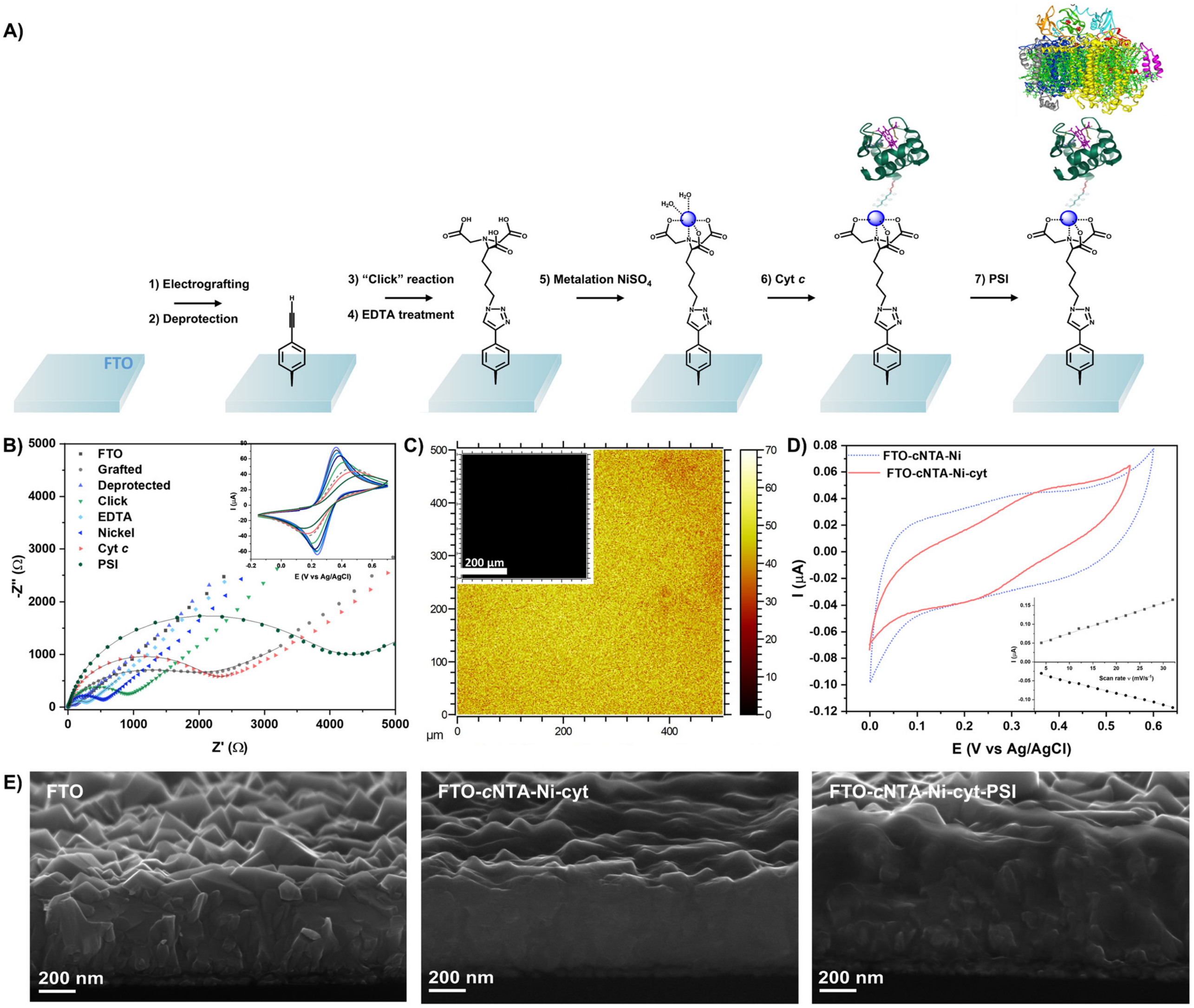

Fig. 1 Synthesis and characterization of the biohybrid electrodes. (A) Schematic representation of the stepwise preparation of functionalized FTO-*c*NTA-Ni-cyt-PSI electrodes. (1) Electrochemical grafting of TMS-N_2 (grafted). (2) TBAF in THF (deprotected). (3) Click chemistry with NTA-N_3 (click). (4) Aqueous solution of EDTA (EDTA). (5) Metalation with $NiSO_4$ (nickel). (6) Biofunctionalization with His$_6$-tagged cytochrome c_{553} (Cyt *c*). (7) Biomolecular recognition with PSI (PSI). (B) Nyquist plot and fitted curves of electrochemical impedance spectra obtained for FTO-*c*NTA-Ni-cyt-PSI electrode at different steps of functionalization. Inset: Corresponding cyclic voltammograms at 100 mV s^{-1} recorded at each step. All measurements were performed with 1 mM 1,1′-ferrocenedimethanol (Fc) in 0.1 M phosphate buffer (pH 7). (C) Atomic mapping by secondary ion mass spectrometry of nickel atoms for the configuration FTO-*c*NTA-Ni. Inset: Corresponding atomic mapping of nickel atoms for the bare FTO substrate. (D) Cyclic voltammetry at 5 mV s^{-1} of functionalized electrode FTO-*c*NTA-Ni with and without immobilized cyt *c*, in 5 mM phosphate buffer (pH 7). Inset: Linear dependency of current (I) *vs.* scan rate (υ) of immobilized cyt *c* in the FTO-*c*NTA-Ni-cyt architecture. (E) Scanning electron microscopy images of the bare FTO, and biohybrid configurations FTO-*c*NTA-Ni-cyt and FTO-*c*NTA-Ni-cyt-PSI, recorded at 75° with a 150.00k× magnification (EHT = 15.00 kV).

Laviron's plot[30] with a value of 0.08 s^{-1} (Fig. S3, ESI†), which is in the lower range of previously reported k_{ET} values for cyt. This rather low value should therefore be improved to allow a fast ET to the photo-oxidized P700$^+$ hole and prevent the internal charge recombination within the P700$^+$F$_B$$^-$ species with a lifetime of 65 ms.[31] Finally, the presence of immobilized PSI was visualized by cross-sectional scanning electron microscopy (SEM) (Fig. 1e and Fig. S4, ESI†) and energy dispersive spectroscopy (EDS) elemental mapping (Fig. S5, ESI†) showing a thicker and smoother bio-organic layer compared to the PSI-devoid controls. The PSI biolayer was additionally observed by confocal fluorescence microscopy depicting ∼2-fold higher fluorescence signal compared to the control samples (Fig. S6, ESI†).

Identification of space-confined Fc in the bio-organic interface

Intrigued by the consistent observation of the Fc signal within the abiotic and biotic architectures after the EIS analyses and considering the capability of analogous Fc counterparts to mediate ET with the photosynthetic bacterial reaction

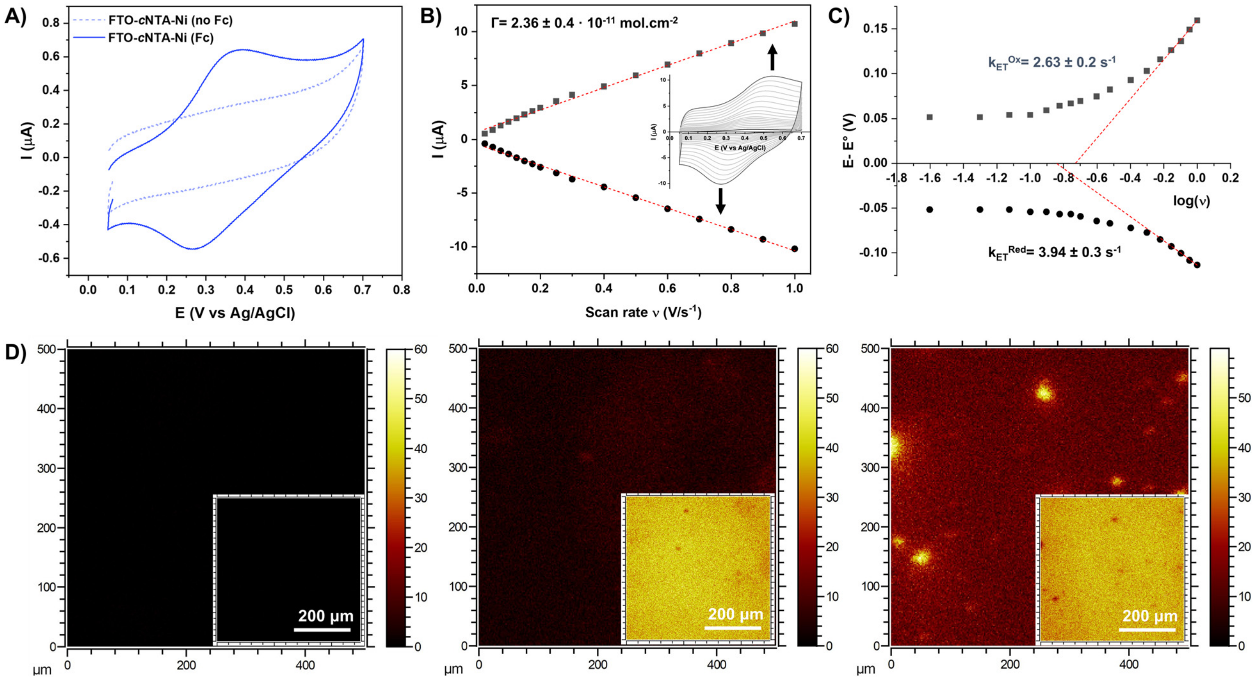

Fig. 2 Detection of space-confined Fc redox centres within the molecular interface. (A) Cyclic voltammetry at 50 mV s^{-1} of functionalized electrode FTO-*c*NTA-Ni with and without entrapped Fc, in 5 mM PB (pH 7). (B) Linear dependency of current (I) *vs.* scan rate (ν) of entrapped Fc in the FTO-*c*NTA-Ni architecture with the calculated surface coverage Γ (value obtained from the average of three independent replicas). Inset: Representative cyclic voltammograms at various scan rates. (C) Corresponding Laviron's plot obtained for the calculation of the k_{ET} parameter (values obtained from the average of three independent replicas). (D) Atomic mapping by SIMS of iron atoms for (left) pristine FTO, (middle) FTO-*c*NTA-Ni without Fc and (right) FTO-*c*NTA-Ni with entrapped Fc. Insets: Corresponding atomic mapping of nickel atoms.

centre,[32,33] a preliminary electrochemical investigation was undertaken with the simplest abiotic architecture, FTO-*c*NTA-Ni. By comparing the electrochemical behaviour of the samples prepared in the presence or absence of the Fc probe (Fig. 2a), a well-defined redox system at $E_{1/2}$ = 0.33 V *vs.* Ag/AgCl corresponding to the Fc^+/Fc couple was identified for the sample characterized by EIS measurements. To exclude the possibility that the signal originates from the residual Fc in the electrolyte solution, the observed redox system was analysed at different scan rates. The resulting $f(\nu) = I$ plot (Fig. 2b) depicts a clear linear dependency, confirming the surface-confined nature of the process. The average surface coverage Γ of 2.36 ± 0.4 × 10^{-11} mol cm^{-2} was obtained for the FTO-*c*NTA-Ni system, which suggests the presence of sparsely-loaded Fc molecules within the interface when compared to the Γ values ranging between 4–7 × 10^{-10} mol cm^{-2} reported for densely packed ferrocene monolayers.[34–36] Interestingly, the extrapolated k_{ET} parameter of entrapped Fc (3.29 s^{-1}; see Fig. 2c) shows a competitive value compared to directly grafted ferrocene analogues (0.8 s^{-1} and 0.4 s^{-1}),[34,35] as well as 40-times higher value than the k_{ET} of immobilized cyt *c* (0.08 s^{-1}).

Complementary to the electrochemical measurements, the SIMS analysis further confirmed and localized the presence of space-confined Fc molecules (Fig. 2d). For the pristine FTO sample, neither Ni nor Fe atoms were observed by the atomic mapping whilst in the case of FTO-*c*NTA-Ni (no Fc) sample, homogeneous detection of Ni was obtained (2.94 × 10^6 counts) without significant traces of Fe. As expected, for the sample FTO-*c*NTA-Ni with confined Fc, both Ni (2.81 × 10^6 counts) and Fe (0.90 × 10^6 counts) atoms were clearly identified. Although several defect spots corresponding to the Fc 'clusters' are visible in the Ni map, the coverage is relatively homogeneous with similar Ni counts as for the Fc-free sample, suggesting that the entrapped Fc molecules are not substituting the Ni ions bound to the NTA moiety but rather may be spread within and beneath the Ni layer of the molecular interface. To verify this hypothesis and obtain in-depth information on the key steps of Fc-entrapment, additional electrochemical analyses were performed to monitor the appearance of confined Fc at each stage of electrode functionalization (Fig. S7, ESI†). Notably, after the EIS measurement on pristine FTO, signals from the surface-confined Fc molecules were identified likely due to their adsorption on the FTO surface *via* hydrogen bonding[37,38] without affecting the overall covalent functionalization, as shown by similar Ni counts recorded by SIMS. Throughout the stepwise functionalization, the variation of the Γ and k_{ET} parameters for Fc indicates a distribution of this redox molecule that is localized in different areas and depths within the interface, as shown by broadening of the CV peaks (at 1 V s^{-1}: ΔE_{FTO} = 168 mV, $\Delta E_{Grafted}$ = 409 mV and ΔE_{Nickel}= 273 mV; see Fig. S7, ESI†). The latter observation implies the occurrence of intermolecular ET between Fc with inhomogeneous chemical environments.[36,39] Overall, these results suggest, together with the observed overlapping of the redox systems for confined Fc and immobilized cyt (Fig. S8, ESI†), improved ET processes across the entire biomolecular nanoarchitecture due to the presence of space-confined Fc acting to boost electron relay pathways between the electrode surface and the photo-generated P700$^+$ hole in PSI.

Enhanced biophotoelectrochemical performance

Recent studies have shown that ferrocene derivatives are capable of replacing the natural cyt *c* as an electron mediator with photoactivated bacterial reaction centre (RC).[32,33] Despite the reported ET between cyt *c* and ferrocenes,[40,41] the combination of these two mediators has not been studied yet, in particular within the PSI-based biomolecular systems.[42] Therefore, the advantages of entrapped Fc within the bio-organic interface of PSI-photocathode were investigated in the context of the photocurrent generation (Fig. 3). As a first step, chopped photochronoamperometric (PCA) measurements with 30 s. cycles of light ON/OFF in aerated 5 mM PB were performed for all the samples at various applied potentials *vs.* Ag/AgCl. A clear improvement of cathodic photocurrent generation was observed for the Fc-confined *vs.* Fc-free biomolecular systems, with the highest enhancement at −300 mV (2.5-fold for FTO-*c*NTA-Ni-cyt-PSI and 1.4-fold FTO-*c*NTA-Ni-cyt; see Fig. 3a and Table S2, ESI†). No significant enhancement of anodic photocurrents was detected in the 200–400 mV potential range, highlighting the beneficial effect of the captured Fc for the directional light-induced ET process.

To emphasize the impact of the confined Fc on the photo-induced ET kinetics, a mathematical model was applied to the normalized PCA curves obtained at 0 mV, whereby the samples reach steady-state photocurrents during the light ON/OFF cycles. The rise of the normalized photocurrent was fitted to a biexponential equation (eqn (1)):

$$I = a \times (1 - \exp(-k_1 t)) + c \times (1 - \exp(-k_2 t)) \qquad (1)$$

where I is the normalized photocurrent, t is the time in seconds, the coefficients a and c represent the contribution of the two phases, and k_1 and k_2 represent the rates of the two exponential raising (Fig. S9 and Table S3 and ESI†).

The two phases presumably account for the different modes of electronic interactions between the abiotic and biotic components of the electrode. The entrapment of Fc influences the contribution of the different modes of interaction between the redox centres and the electrode surface in both types of nanoassemblies. From the photocurrent profiles and the fitting procedure (Fig. S9 and ESI†), an apparent photocurrent kinetic

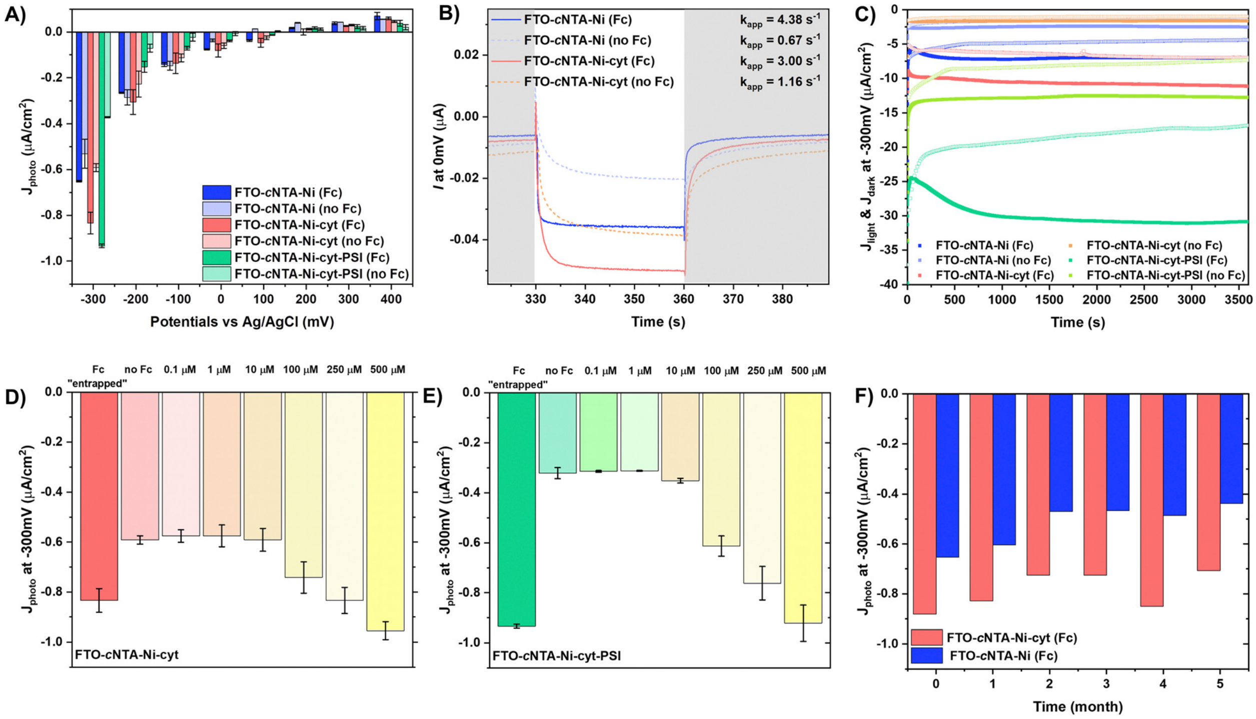

Fig. 3 Photoelectrochemical performances. (A) Photocurrent densities of functionalized electrodes recorded within 30 s. cycles of light ON/OFF in 5 mM phosphate buffer at different applied potentials (100 mW cm^{-2} white light source). (B) Representative photochronoamperometric curve profiles recorded at 0 V *vs.* Ag/AgCl of functionalized electrodes with and without entrapped Fc, in 5 mM phosphate buffer (pH 7). Inset: Apparent photocurrent kinetics rates k_{app} estimated from the fitting parameters obtained with a biexponential rise to maximum kinetic model (Fig. S9 and Table S3, ESI†). (C) Long-term chronoamperometric measurements at −300 mV *vs.* Ag/AgCl under 1 hour of light (full square) and dark conditions (empty square). (D) Photocurrent densities obtained at −300 mV *vs.* Ag/AgCl during chopped irradiation of FTO-*c*NTA-Ni-cyt with entrapped Fc and without entrapped Fc in the presence of increased concentration of diffusive Fc in the aerated 5 mM PB electrolyte. (E) Photocurrent densities obtained at −300 mV *vs.* Ag/AgCl during chopped irradiation of FTO-*c*NTA-Ni-cyt-PSI with entrapped Fc and without entrapped Fc in the presence of increased concentration of diffusive Fc in aerated 5 mM PB electrolyte. (F) Stability test over 5 months of the photocurrent density at −300 mV obtained through chopped irradiation for FTO-*c*NTA-Ni and FTO-*c*NTA-Ni-cyt with entrapped Fc.

rate k_{app} can be derived. The values of k_{app} shown in Fig. 3b indicate a faster photo-induced electron extraction in the Fc-confined systems. No surface charge recombination was detected during the dark phase.[43]

Consequently, the presence of entrapped Fc leads to a considerable improvement of the overall photocurrent density (J_{photo}) produced at −300 mV during prolonged 1 hour irradiation (Fig. 3c and Table S4, ESI†). The Fc-confined abiotic and cyt-based bio-organic interfaces showed an improvement factor for the photocurrent output of 2.7 (J_{photo} = 2.67 μA cm^{-2}) and 6.3 (J_{photo} = 4.19 μA cm^{-2}), respectively. For the PSI-based photocathode, an enhancement factor of 2.6 was recorded reaching an outstanding photocurrent response of 14 μA cm^{-2} compared to analogous planar PSI-based photocathodes, even surpassing recent systems based on 3D nanostructured materials (Table S5, ESI†).

To further confirm the role of Fc as a redox mediator despite its non-ideal absorption overlap with PSI transitions (Fig. S10, ESI†),[42] chopped PCA measurements were performed for the Fc-free biophotocathodes with increasing concentrations of freely-diffusive Fc, and compared to the Fc-confined counterparts. As shown in Fig. 3d and e (Fig. S11, ESI†), the photocurrent response of Fc-free biomolecular systems started to increase from the addition of 100 μM freely-diffusive Fc, whilst lower concentrations were ineffective. Remarkably, Fc-confined analogues with an equivalent concentration of ∼1 nM yielded a photocurrent response similar to Fc-free systems with 500 μM of freely-diffusing Fc, exacerbating the advantage of space-confining the mediator to maximize the efficiency of forward ET and reduce competitive short-circuiting and back reaction processes.[44]

To shed light on the ET thermodynamics in these systems, the energy diagram was constructed by combining the converted redox potential[45] of various species obtained in solution (cyt *c*[46] and Fc) with the published energy levels of PSI[47] and molecular oxygen[48] (see Fig. 4). Following photoexcitation of PSI, the charge-separated state $P700^{+}F_{B}^{-}$ is formed. In the presence of molecular oxygen acting as an electron acceptor, an ET from the F_{B}^{-} to O_2 occurs whilst the ground state of the photoreactive centre of PSI (P700) is regenerated by ET from cyt *c*. The oxidized cyt *c* is finally reduced by ET from the electrode, closing the circuit and generating a cathodic photocurrent. In the case of the Fc-free biophotocathode, the interfacial ET kinetics between the electrode and cyt *c* is rather sluggish (k_{ET} = 0.08 s^{-1}), favouring partial internal charge recombination between $P700^{+}$ and F_{B}^{-}; therefore, resulting in lower photocurrent production.

However, we propose that in the case of the Fc-enriched system, the space-confined Fc behaves as an efficient electron mediator, as evidenced by the faster interfacial ET kinetics (k_{ET} = 3.29 s^{-1}) and improved photo-induced ET from the electrode to cyt *c* (k_{app} rates). Ultimately, both effects result in the significantly enhanced cathodic photocurrent output in the presence of entrapped Fc. Interestingly, in a previously reported RC-based biohybrid system, covalently bound ferrocenes analogues were inefficient in improving the photocurrent generation under monochromatic irradiation in the absence of additional diffusive mediators.[33] Therefore, we hypothesize that in the systems reported in this study, efficient ET mediation is achieved between cyt *c* and electrode surface due to the mobility of the space-confined Fc serving as an electron shuttle. Another implication is that the full spectrum irradiation photosensitizes the Fc, which promotes ET from photoexcited Fc to cyt *c*. We propose that both processes may synergistically enhance photo-induced ET. Complementary investigations are currently underway to determine the exact molecular mechanism of the ET processes occurring in the Fc-confined systems, whilst preliminary UV-visible data in solution confirmed the possible cyt *c* reduction by Fc (Fig. S12, ESI†).

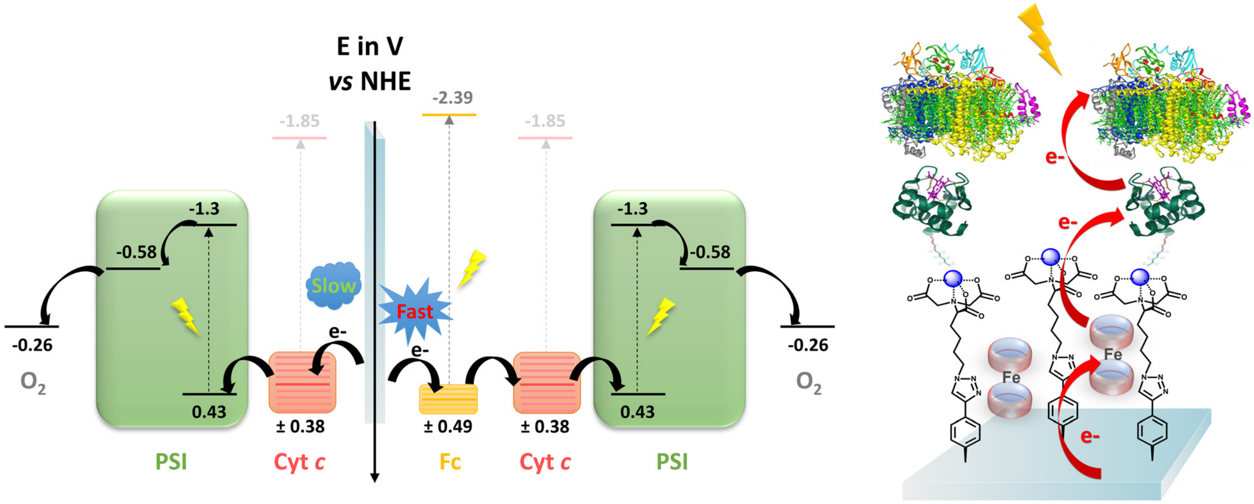

Fig. 4 Proposed mechanism of space-confined mediation of ET. Calculated energy diagram and the corresponding proposed photo-induced ET processes occurring in the bioarchitecture FTO-*c*NTA-Ni-cyt-PSI with and without entrapped Fc (left). The most favorable ET pathways are shown with dark arrows. On the right is shown the schematic representation of the photo-induced ET through space-confined Fc in the biohybrid system FTO-*c*NTA-Ni-cyt-PSI.

Finally, the long-term photocurrent stabilities of the Fc-confined abiotic and cyt-based systems were investigated weekly by performing chopped PCA measurements at −300 mV in fresh aerated 5 mM PB electrolyte (Fig. 3f and Fig. S13, ESI†). The results demonstrate the long-term stability of the nanosystems up to 5 months, whilst the apparent decrease of photocurrent density beyond this period could be explained by the progressive release of the confined Fc or its degradation by oxygen[49] (Fig. S14, ESI†).

Conclusions

In this study, we report a simple, yet breakthrough approach for the efficient electrical wiring of photoenzymes with transparent electrodes resulting in significant enhancement of the cathodic photocurrent generation, by the application of space-confined, non-toxic mediators used as redox shuttle at the bio-organic interface. This approach can universally be applied to various biological photoactive systems for solar conversion,[25,26,32,33] as well as to any electroactive enzymes for specific bioelectrocatalysis[10,50] and biosensing applications.[51]

The biophotocathode of the present study was constructed with two photosynthetic molecular interactors, cyt *c* and PSI to ensure maximization of anisotropic ET by applying rationally designed covalent metalorganic interface for the controlled orientation and electrical wiring of the PSI biophotocatalyst.

The discovery of the space-confined Fc mediator system shows for the first time the application of this innocuous redox molecule as electron shuttle within the bio-organic interface. Such an approach leads to significantly enhanced directional ET and the overall photocurrent output of 14 μA cm^{-2}. Importantly, the Fc-confined biohybrid photocathodes (∼1 nM Fc) outperformed the Fc-free counterparts even in the presence of freely diffusive Fc (up to 500 μM). Thus, the approach offers a true milestone in the quest for developing viable solar conversion systems whilst avoiding the limitations of mass transfer and the necessity of applying high amounts of toxic mediators. Last but not least, the investigation of the long-term performance of the system described in the present study revealed the stability of photocurrent generation for up to 5 months for the Fc-confined system even in the presence of oxygen, which can be further improved by application of anoxic conditions.

Overall, the concept of space-confined mediators presented in this study can be successfully applied for the rational design of the bio-organic interface between electroactive molecular machines and synthetic electrode materials, opening a new avenue to eliminate the critical performance bottlenecks in the present-day biohybrid systems.[10,50,52,53] Space-confined ET mediation provides a sustainable approach to maximize the efficiency of ET processes within the abiotic–biotic interface, avoiding the detrimental effects and competitive interference of external mediators in a range of applications in biophotovoltaics, solar fuels production, biocatalysis and biosensing. As such, the concept paves the way for the advancement toward long-term high performance biomolecular technologies for solar conversion and bioelectronics.

Experimental

General materials

All chemical reagents and solvents used for the synthesis were purchased from commercial sources (Merk, Acros, and VWR) and were used without further purification unless otherwise noted. FTO glass substrates were purchased from Sigma Aldrich (30 mm × 30 mm and 2.2 mm thickness). Prior to use, FTO electrodes were pre-cut to a size of 15 × 15 mm for all subsequent modification steps. The 4-((trimethylsilyl)ethynyl)benzenediazonium tetrafluoroborate (TMS-N_2) and N^{α},N^{α}-bis(carboxymethyl)-L-azido-lysine hydrochloride (NTA-N_3) were synthesized as previously described.[26] His$_6$-tagged cytochrome c_{553} (19AA protein)[54] and photosystem I from *C. merolae*[13] were prepared and purified in our laboratory as previously reported. UV-visible absorption spectra were recorded at room temperature between 300 and 800 nm using a UV-1800 spectrophotometer (Shimadzu).

Surface modification

Fc-free functionalization procedure. The stepwise construction of the metalorganic interface was done as previously described.[26] The pristine FTO was cleaned in an acetone bath for 1 min by ultrasonication and left to dry before being inserted in the electrochemical cell for the entire functionalization process. TMS-N_2 (2.2 mM) electrografting was performed in degassed 0.1 M tetrabutylammonium hexafluorophosphate (NBu_4PF_6) in acetonitrile *via* cyclic voltammetry between +500 mV to −500 mV *vs.* Ag/AgCl at a scan rate of 50 mV s^{-1} (1 cycle). After cleaning with acetonitrile and tetrahydrofuran (THF), the surface was immersed in a tetrabutylammonium fluoride (TBAF) solution (50 mM in THF) for 5 min. The electrochemical cell was rinsed with THF and water before adding an argon-saturated solution of NTA-N_3 (0.4 mM in water), followed by a mixture of 100 μL of tris(benzyltriazolylmethyl)amine (TBTA) in DMSO (0.10 mM) and 200 μL of $CuSO_4$ in water (0.04 mM). Additional argon bubbling for 15 min was done and 100 μL of sodium ascorbate solution in water (1.5 mM) was added to the cell to run the click chemistry reaction overnight under an inert atmosphere. After the cleaning step with water, an ethylenediaminetetraacetic acid (EDTA) solution (2.5 mM in water) was added to the cell for 20 min. The cell was then rinsed with water and the metalation with $NiSO_4{\cdot}7H_2O$ was performed in a 0.1 M aqueous solution for 1 hour. Following cleaning steps with water, the surface was incubated with a 30 μM cyt *c* solution in 5 mM phosphate buffer (pH 7) for 2 h at room temperature. Finally, after removal of the unbound cyt *c*, a 0.2 μM PSI solution in 5 mM phosphate buffer (pH 7) was dropcasted on the surface to react overnight at 4 °C in the dark.

Fc-confined functionalization procedure. For the Fc-enriched systems, at each stage of the functionalization, the electrochemical cell was additionally cleaned with a copious amount of water before adding 8 mL of a 1 mM 1,1′-ferrocenedimethanol solution in 0.1 M phosphate buffer (pH 7). The solution was degassed for 20 min before running the electrochemical analyses (cyclic voltammetry and electrochemical impedance spectroscopy), followed by copious rinsing with water and with the solvent used for the next functionalization step.

Electrochemistry

Electrochemical experiments were performed with a Metrohm Autolab B.V. potentiostat/galvanostat in a custom-made Teflon three-electrode cell under argon atmosphere, using a glassy carbon rod as the counter electrode (CE) and an Ag/AgCl (3 M KCl) reference electrode. The FTO surface was used as a working electrode (WE) connected with a conductive adhesive copper tape (6.4 mm width, 1181, 3 M) to provide electrical contact. The geometric surface area of the analysed samples was calculated as 0.3848 cm^2 based on the FFKM O-ring used as a hermetic seal between the surface and the electrolyte (8 mL). Cyclic voltammetry (CV) and electrochemical impedance measurements (EIS) were conducted in 20 min argon-saturated 0.1 M phosphate buffer (pH 7) with 1 mM 1,1′-ferrocenedimethanol at a scan rate of 100 mV s^{-1} (CV) and at a frequency range from 0.01 Hz to 0.1 MHz (EIS). The Z-View 2 software was used to fit the impedance data with an equivalent circuit. Complementary CV analyses were performed in deoxygenated 5 mM phosphate buffer (pH 7). The surface coverage Γ (mol cm^{-2}) was calculated from the slope of the line $f(\nu) = I$ using the following eqn (2), where I is the current peak intensity, n is the number of electrons involved in the process ($n = 1$), F is the Faraday constant, R is the gas constant, T is the temperature (298 K), ν is the scan rate and A is the surface (0.3848 cm^2). The resulting surface coverage values are in good agreement with the surface coverage values obtained at low scan rates from the corrected faradaic current (I_p) or from the equation $\Gamma = \Pi/AnF\upsilon$, where Π is the area of the redox peak (Tables S6 and S7, ESI†).

$$I = \left(\frac{n^2 \times F^2}{4 \times R \times T}\right)\Gamma \times \nu \times A \qquad (2)$$

Photoelectrochemical experiments were performed using a KL 2500 LCD halogen white light source (Schott) with a light intensity of 100 mW cm^{-2}. Photochronoamperometric experiments were performed in aerobic conditions at room temperature with 5 mM phosphate buffer (pH 7) as the electrolyte, unless otherwise specified. Before each sample measurement, the open circuit potential (OCP) was recorded under dark conditions until a stable potential was achieved. During chopped photochronoamperometric measurements, samples were illuminated at different potentials (*vs.* Ag/AgCl) with 30 s. 'light ON/OFF' periods, whilst for continuous chronoamperometric measurements, samples were exposed to dark or light conditions for 1 hour at a specified potential. To extract the photo-induced ET kinetics, the normalized photochronoamperometric curves obtained at 0 mV were fitted to a biexponential rise to maximum using Levenberg–Marquardt algorithm (least-squares curve fitting)[55] implemented in a locally developed software, with the following eqn (3), where I is the normalized photocurrent, t is the time in seconds and the coefficients a and c represents the contribution of the two phases while k_1 and k_2 represent the rate of the two exponential raising. The apparent photocurrent kinetic rates k_app were extrapolated from the obtained exponential rate (k_1 and k_2) and their respective contribution coefficient (a and c) following eqn (4).

$$I = a \times (\mathrm{e}^{-k_1 \times t}) + c \times (\mathrm{e}^{-k_2 \times t}) \qquad (3)$$

$$k_\text{app} = a \times k_1 + c \times k_2 \qquad (4)$$

The chopped photochronoamperometric measurements with freely-diffusive Fc were performed at −300 mV *vs.* Ag/AgCl with the Fc-free electrodes by replacing the electrolyte solution successively with Fc solutions prepared at the specified concentration. For the long-term photocurrent stability analyses, the electrodes were kept in the electrochemical cell with aerated 5 mM phosphate buffer electrolyte in the fridge (dark, 4 °C) between each weekly photochronoamperometric measurement performed at −300 mV *vs.* Ag/AgCl with freshly-changed aerated 5 mM phosphate buffer electrolyte.

Determination of the energy diagram:[45] from the converted redox potentials of cyt *c* and Fc obtained in solution *vs.* the SCE reference electrode (by removing 39 mV to the values *vs.* Ag/AgCl), the energy of the highest occupied molecular orbital (HOMO) can be calculated. The respective values of −4.89 eV (+0.38 V *vs.* NHE) and −4.98 eV (+0.49 V *vs.* NHE) related to the vacuum energy level were determined using eqn (5) with an energy of −4.74 eV for SCE with respect to the zero-vacuum level. Considering the 0–0 transition energy ΔE^{00} of cyt *c* and Fc (λ^{00} cyt *c* = 553 nm) (Fig. S10, ESI†) and λ^{00} Fc = 431 nm (Fig. S10, ESI†), the energy of the lowest occupied molecular level (LUMO) can be estimated at −2.64 eV (−1.85 V *vs.* NHE) and −2.63 eV (−2.39 V *vs.* NHE), respectively, related to the vacuum energy level using the eqn (5) and (6).

$$E_\text{HOMO}\ (\text{eV}) = -4.74 - E_{1/2} \qquad (5)$$

$$\Delta E^{00} = E_\text{LUMO} - E_\text{HOMO} = \frac{1240}{\lambda^{00}} \qquad (6)$$

Secondary ion mass spectrometry

Distribution of ions over the sample surface was obtained with a time of flight secondary ion mass spectrometry (TOF-SIMS). The measurements were performed on a TOF-SIMS.5 spectrometer (ION-TOF GmbH, Germany) operating in $\text{Bi}_3{}^+$ mode. The as-received, samples were transferred without special pretreatment to the analytical chamber. The base pressure in the chamber was below 2×10^{-9} mbar. Operating mode of the instrument was spectroscopy at 30 keV energy and 0.45 pA $\text{Bi}_3{}^+$ ion current conditions. Analyses were done over 500 μm × 500 μm area. The internal mass calibration was performed using mass a series of ions from Mg^+ up to Sn^+.

Fluorescence confocal microscopy

The electrodes were analysed using a Zeiss LSM700 laser scanning confocal microscopy following the protocol implemented in the previously published study.[56] Briefly, the fluorescence maps were generated setting the excitation wavelength at 636 nm, while the emission was recorded at 669 nm with a detection wavelength between 644 and 694 nm. The acquired pictures, with a size of 640 μm, were taken using the Z-stack mode using a 10× objective (NA 0.3) with a pixel size of 0.63 μm and a pinhole size of 1 airy unit (AU). The sets of images taken at a different depth of focus were overlapped to generate a 2.5-dimensional (2.5 D) fluorescence map with a greater depth of field (DOF) than any of the single source images using ZEN 2.6 lite software.

Scanning electron microscopy

The cross-sectional imaging of the samples was performed using scanning electron microscopy (SEM) with a Zeiss Sigma microscope equipped with a field emission cathode (HV FE) with in-lens secondary electron and backscattered electron detectors. The images were taken by combining signals from the two detectors at a 50 : 50 percent ratio in order to visualize the fine surface features and enhance the contrast. Energy dispersive spectroscopy (EDS) elemental mapping measurements were carried out in SEM Zeiss Sigma HV at 90 degrees with Bruker Quantax microanalysis system equipped with an XFlash detector. The data were collected and analysed using Bruker ESPRIT software.

Author contributions

MJ: conceptualization, investigation, formal analysis, methodology, funding acquisition, project administration, validation, visualization, writing – original draft. MI: investigation, formal analysis, validation, writing – review & editing. PW, MS: investigation, formal analysis, writing – review & editing. MT, RJ: formal analysis, validation, writing – review & editing. JK: conceptualization, funding acquisition, project administration, supervision, writing – review & editing.

Data availability

The data supporting this article have been included as part of the ESI.†

Conflicts of interest

There are no conflicts to declare.

Acknowledgements

We thank Konrad Krzyżak from the Łukasiewicz Research Network, Institute of Microelectronics and Photonics for the cutting of FTO substrates. MJ and JK acknowledge the financial support from the Polish National Science Centre (OPUS14 grant no. UMO-2017/27/B/ST5/00472 to JK and SONATA18 grant no. UMO-2022/47/D/ST5/03168 to MJ). MJ acknowledges the financial support from the Excellence Initiative Research University program of the University of Warsaw (New Ideas 2A POB I grant no. BOB-IDUB-622-202/2022).

References

1 J. Barber and B. Andersson, *Nature*, 1994, **370**, 31–34.

2 A. Fujishima and K. Honda, *Nature*, 1972, **238**, 37–38.

3 N. S. Lewis, *Nat. Nanotechnol.*, 2016, **11**, 1010–1019.

4 S. D. Tilley, *Adv. Energy Mater.*, 2019, **9**, 1–13.

5 B. Qiu, M. Du, Y. Ma, Q. Zhu, M. Xing and J. Zhang, *Energy Environ. Sci.*, 2021, **14**, 5260–5288.

6 E. A. Reyes Cruz, D. Nishiori, B. L. Wadsworth, N. P. Nguyen, L. K. Hensleigh, D. Khusnutdinova, A. M. Beiler and G. F. Moore, *Chem. Rev.*, 2022, **122**, 16051–16109.

7 Z. Chen, H. Zhang, P. Guo, J. Zhang, G. Tira, Y. J. Kim, Y. A. Wu, Y. Liu, J. Wen, T. Rajh, J. Niklas, O. G. Poluektov, P. D. Laible and E. A. Rozhkova, *J. Am. Chem. Soc.*, 2019, **141**, 11811–11815.

8 Z. Chen, G. De Queiros Silveira, X. Ma, Y. Xie, Y. A. Wu, E. Barry, T. Rajh, H. C. Fry, P. D. Laible and E. A. Rozhkova, *Angew. Chem., Int. Ed.*, 2019, **58**, 4896–4900.

9 P. Wang, N. M. Dimitrijevic, A. Y. Chang, R. D. Schaller, Y. Liu, T. Rajh and E. A. Rozhkova, *ACS Nano*, 2014, **8**, 7995–8002.

10 N. Kornienko, J. Z. Zhang, K. K. Sakimoto, P. Yang and E. Reisner, *Nat. Nanotechnol.*, 2018, **13**, 890–899.

11 X. Fang, S. Kalathil and E. Reisner, *Chem. Soc. Rev.*, 2020, **49**, 4926–4952.

12 N. S. Weliwatte and S. D. Minteer, *Joule*, 2021, 1–29.

13 P. Haniewicz, M. Abram, L. Nosek, J. Kirkpatrick, E. El-Mohsnawy, J. D. Janna Olmos, R. Kouril and J. M. Kargul, *Plant Physiol.*, 2018, **176**, 1433–1451.

14 A. Badura, T. Kothe, W. Schuhmann and M. Rögner, *Energy Environ. Sci.*, 2011, **4**, 3263–3274.

15 A. H. Teodor and B. D. Bruce, *Trends Biotechnol.*, 2020, **38**, 1329–1342.

16 K. R. Stieger, S. C. Feifel, H. Lokstein, M. Hejazi, A. Zouni and F. Lisdat, *J. Mater. Chem. A*, 2016, **4**, 17009–17017.

17 K. Peters, H. N. Lokupitiya, D. Sarauli, M. Labs, M. Pribil, J. Rathouský, A. Kuhn, D. Leister, M. Stefik and D. Fattakhova-Rohlfing, *Adv. Funct. Mater.*, 2016, **26**, 6682–6692.

18 A. Mershin, K. Matsumoto, L. Kaiser, D. Yu, M. Vaughn, M. K. Nazeeruddin, B. D. Bruce, M. Graetzel and S. Zhang, *Sci. Rep.*, 2012, **2**, 1–7.

19 G. Leblanc, G. Chen, E. A. Gizzie, G. K. Jennings and D. E. Cliffel, *Adv. Mater.*, 2012, **24**, 5959–5962.

20 D. Yu, M. Wang, G. Zhu, B. Ge, S. Liu and F. Huang, *Sci. Rep.*, 2015, **5**, 1–9.

21 A. Badura, D. Guschin, T. Kothe, M. J. Kopczak, W. Schuhmann and M. Rögner, *Energy Environ. Sci.*, 2011, **4**, 2435–2440.

22 F. Zhao, A. Ruff, M. Rögner, W. Schuhmann and F. Conzuelo, *J. Am. Chem. Soc.*, 2019, **141**, 5102–5106.

23 O. Yehezkeli, R. Tel-Vered, D. Michaeli, R. Nechushtai and I. Willner, *Small*, 2013, **9**, 2970–2978.

24 A. Efrati, C.-H. Lu, D. Michaeli, R. Nechushtai, S. Alsaoub, W. Schuhmann and I. Willner, *Nat. Energy*, 2016, **1**, 1–8.

25 M. Kiliszek, E. Harputlu, M. Szalkowski, D. Kowalska, C. G. Unlu, P. Haniewicz, M. Abram, K. Wiwatowski, J. Niedziółka-

Jönsson, S. MaćKowski, K. Ocakoglu and J. Kargul, *J. Mater. Chem. A*, 2018, **6**, 18615–18626.

26 M. Jacquet, S. Osella, E. Harputlu, B. Pałys, M. Kaczmarek, K. Nawrocka, A. A. Rajkiewicz, M. Kalek, P. Michałowski, G. C. Unlu, W. Lisowski, M. Pisarek, K. Kazimierczuk, K. Ocakoglu, A. Więckowska and J. Kargul, *Chem. Mater.*, 2022, **34**, 3744–3758.

27 K. R. Stieger, S. C. Feifel, H. Lokstein and F. Lisdat, *Phys. Chem. Chem. Phys.*, 2014, **16**, 15667–15674.

28 A. Efrati, R. Tel-Vered, D. Michaeli, R. Nechushtai and I. Willner, *Energy Environ. Sci.*, 2013, **6**, 2950–2956.

29 T. Pajkossy and R. Jurczakowski, *Curr. Opin. Electrochem.*, 2017, **1**, 53–58.

30 E. Laviron, *J. Electroanal. Chem.*, 1979, **100**, 263–270.

31 V. Kurashov, M. Gorka, G. E. Milanovsky, T. W. Johnson, D. A. Cherepanov, A. Y. Semenov and J. H. Golbeck, *Biochim. Biophys. Acta, Bioenerg.*, 2018, **1859**, 1288–1301.

32 S. M. Mirvakili, J. E. Slota, A. R. Usgaocar, A. Mahmoudzadeh, D. Jun, M. N. Mirvakili, J. T. Beatty and J. D. W. Madden, *Adv. Funct. Mater.*, 2014, **24**, 4789–4794.

33 R. Caterino, R. Csiki, A. Lyuleeva, J. Pfisterer, M. Wiesinger, S. D. Janssens, K. Haenen, A. Cattani-Scholz, M. Stutzmann and J. A. Garrido, *ACS Appl. Mater. Interfaces*, 2015, **7**, 8099–8107.

34 C. Fontanesi, E. Da Como, D. Vanossi, M. Montecchi, M. Cannio, P. C. Mondal, W. Giurlani, M. Innocenti and L. Pasquali, *Sci. Rep.*, 2019, **9**, 1–7.

35 P. Fortgang, T. Tite, V. Barnier, N. Zehani, C. Maddi, F. Lagarde, A. S. Loir, N. Jaffrezic-Renault, C. Donnet, F. Garrelie and C. Chaix, *ACS Appl. Mater. Interfaces*, 2016, **8**, 1424–1433.

36 R. A. Wong, Y. Yokota, M. Wakisaka, J. Inukai and Y. Kim, *J. Am. Chem. Soc.*, 2018, **140**, 13672–13679.

37 N. Kurapati, P. Pathirathna, R. Chen and S. Amemiya, *Anal. Chem.*, 2018, **90**, 13632–13639.

38 Z. Cao, Z. Song, F. Liang, X. An, K. K. Al-Quraishi, M. Wang, J. Chen, D. Ding and Y. Yang, *RSC Adv.*, 2020, **10**, 17438–17443.

39 R. P. Gautam and C. J. Barile, *J. Phys. Chem. C*, 2021, **125**, 8177–8184.

40 M. J. Carney, J. S. Lesniak, M. D. Likar and J. R. Pladziewicz, *J. Am. Chem. Soc.*, 1984, **106**, 2565–2569.

41 S. J. Sadeghi and A. E. G. Cass, *Biochem. Soc. Trans.*, 1995, **23**, 995.

42 G. Chen, G. LeBlanc, G. K. Jennings and D. E. Cliffel, *J. Electrochem. Soc.*, 2013, **160**, H315–H320.

43 D. Buesen, T. Hoefer, H. Zhang and N. Plumeré, *Faraday Discuss.*, 2019, **215**, 39–53.

44 P. Wang, F. Zhao, A. Frank, S. Zerria, A. Lielpetere, A. Ruff, M. M. Nowaczyk, W. Schuhmann and F. Conzuelo, *Adv. Energy Mater.*, 2021, **11**, 2102858.

45 X. Chen, Y. C. Dai, Z. B. Zheng and K. Z. Wang, *J. Colloid Interface Sci.*, 2013, **402**, 107–113.

46 M. Jacquet, M. Izzo, S. Osella, S. Kozdra, P. P. Michalowski, D. Golowicz, K. Kazimierczuk, M. T. Gorzkowski, A. Lewera, M. Teodorczyk, B. Trzaskowski, R. R. Jurczakowski, D. T. Gryko, J. Kargul, P. P. Michałowski, D. Gołowicz, K. Kazimierczuk, M. T. Gorzkowski, A. Lewera, M. Teodorczyk, B. Trzaskowski, R. R. Jurczakowski, D. T. Gryko and J. Kargul, *Nanoscale*, 2021, **13**, 9773–9787.

47 N. Nelson and C. F. Yocum, *Annu. Rev. Plant Biol.*, 2006, **57**, 521–565.

48 X. Chen, L. Gao, Z. Zheng and K. Wang, *Mater. Res. Bull.*, 2013, **48**, 595–602.

49 G. Zotti, G. Schiavon, S. Zecchin and D. Favretto, *J. Electroanal. Chem.*, 1998, **456**, 217–221.

50 M. Grattieri, K. Beaver, E. M. Gaffney, F. Dong and S. D. Minteer, *Chem. Commun.*, 2020, **56**, 8553–8568.

51 M. Riedel, N. Sabir, F. W. Scheller, W. J. Parak and F. Lisdat, *Nanoscale*, 2017, **9**, 2814–2823.

52 X. Chen, J. M. Lawrence, L. T. Wey, L. Schertel, Q. Jing, S. Vignolini, C. J. Howe, S. Kar-Narayan and J. Z. Zhang, *Nat. Mater.*, 2022, **21**, 811–818.

53 E. R. Clifford, R. W. Bradley, L. T. Wey, J. M. Lawrence, X. Chen, C. J. Howe and J. Z. Zhang, *Chem. Sci.*, 2021, **12**, 3328–3338.

54 J. D. J. Olmos, P. Becquet, D. Gront, J. Sar, A. Dąbrowski, G. Gawlik, M. Teodorczyk, D. Pawlak and J. Kargul, *RSC Adv.*, 2017, **7**, 47854–47866.

55 P. R. Bevington and D. K. Robinson, *Data reduction and error analysis for the physical sciences*, McGraw-Hill, USA, 1992.

56 M. Izzo, M. Jacquet, T. Fujiwara, E. Harputlu, R. Mazur, P. Wróbel, T. Góral, C. Gokhan Unlu, K. Ocakoglu, S. Miyagishima and J. Kargul, *Int. J. Mol. Sci.*, 2021, **22**, 8396.